



Microstructure and texture evolution during thermomechanical processing of β -quenched Zr

D.G. Leo Prakash,^{a,b,*} M. Preuss,^b M. Dahlbäck^c and J. Quinta da Fonseca^{b,*}

^aMaterials Research Centre, College of Engineering, University of Swansea, Swansea SA2 8PP, UK

^bManchester Materials Science Centre, The University of Manchester, Grosvenor Street, Manchester M1 7HS, UK

^cWestinghouse Electric Sweden, SE-72163 Västerås, Sweden

Received 3 July 2014; revised 16 December 2014; accepted 18 December 2014

Abstract—The evolution of microstructure and texture of an α -Zr alloy during thermomechanical processing was investigated, starting from the β -quenched microstructure. The material was rolled at 550 °C to reductions of 10, 20, 40 and 60%, and held at 550 °C for 24 h. EBSD was used to measure the texture at the different reductions and characterize the microstructural evolution, and crystal plasticity finite element modelling was used as a theoretical framework to help understand the changes in texture observed. Our results show that slip, twinning and recrystallization all play a role in the microstructure development during hot rolling. Their contribution to texture development, lamellae break-up and the ultimate development of a bimodal microstructure are discussed.

© 2015 Acta Materialia Inc. Published by Elsevier Ltd. This is an open access article under the CC BY license (<http://creativecommons.org/licenses/by/4.0/>).

Keywords: Zirconium; Thermomechanical processing; Microstructure; Texture evolution; Crystal plasticity

1. Introduction

Zirconium and its alloys are used as cladding and channel material for fuel assemblies in the nuclear power generation industry [1]. Their excellent corrosion resistance and low thermal neutron capture make them ideal for use in nuclear reactors. The best in-reactor performance of a Zr alloy relies on the development of ideal microstructures through thermomechanical processing. For instance, second phase particle size affects in-reactor corrosion performance, while irradiation-induced creep and growth as well as hydride precipitation are all strongly influenced by the texture of the low temperature α phase (hexagonal close-packed) [2–8]. However, despite the importance of having a controlled and homogeneous microstructure, our knowledge of how this is achieved during processing is entirely empirical, whereas the physical processes responsible for the microstructural evolution are only partially understood. This is in contrast with other important engineering metals, like aluminium, where research on the fundamental mechanisms of microstructure evolution has led to through-process models that are used to optimize and control their processing. Here we present the results of a

study on the microstructural evolution during the hot rolling of a β -quenched zirconium alloy, ZIRLO™, and interpret it in terms of slip and twin activity as well as recovery and recrystallization. The aim was to develop the understanding that will make it possible to construct predictive models of microstructure evolution during processing.

During processing of Zr alloys, the material is usually homogenized in the high temperature β phase (body-centred cubic) at the start. The β heat treatment generates large β grains, from which an α lamellae microstructure develops on cooling. This relatively coarse microstructure is subsequently broken up by thermomechanical processing, forging and rolling, to produce the required final equiaxed microstructure. Previous work on hot compression in the $\alpha + \beta$ phase region of Zr–2.5Nb (650–950 °C) [9] and upper α phase region in Zircaloy-4 (500–750 °C) [10,11] has suggested that the lamellae break-up originates from subgrain formation, similar to what has been reported for $\alpha + \beta$ Ti alloys [12] and that deformation of the β phase is crucial to lamellae break-up. However, no detailed study of lamellae break-up in single-phase lamellar microstructures has been reported. In particular, what happens after relatively small deformations and high temperatures has not been investigated, ignoring the potential role deformation twinning could play in lamellae break-up. In fact, although twinning is sometimes observed in material deformed at room and elevated temperatures [13–18] it is often ignored as a cold [19–21] or hot deformation mechanism during processing. This is not a trivial consideration: if twinning

* Corresponding author at: Materials Research Centre, College of Engineering, University of Swansea, Swansea SA2 8PP, UK. Tel.: +44 1792602573; e-mail addresses: l.prakash@swansea.ac.uk; Joao.Fonseca@manchester.ac.uk

is important in the microstructure development during thermomechanical processing, then it must be included in deformation processing models, such as those based on crystal plasticity. A secondary aim of this paper is to determine whether twinning is an active deformation mechanism at these temperatures and how, if at all, it affects microstructural development.

2. Experimental procedure

ZIRLO™ is an advanced Zr alloy that was developed by Westinghouse to replace the traditional Zircaloy-4 as cladding material in pressurized water reactors. This Zr–Nb–Sn–Fe alloy system belongs to a class of modern Nb containing Zr alloys that have demonstrated enhanced in-reactor performance [22]. ZIRLO™ material was provided by Westinghouse in the form of hot rolled and recrystallized plate. The nominal chemical composition of this material is given in Table 1. As a first step, the material was heat treated at 1050 °C for 30 min followed by water quenching to achieve a starting material with a β transformed acicular α structure. Prior to rolling, the 19 mm thick ZIRLO™ samples were annealed at 550 °C (single α phase regime) for 40 min. Subsequently, the samples were hot rolled again at 550 °C to 10, 20, 40 and 60% reduction using 250 mm diameter rolls operating at a roll surface speed of 150 mm s⁻¹ with light oil lubrication. Between each rolling pass, 1–2 min inter-pass reheating was used to ensure the work temperature was maintained at 550 °C. Subsequently, the rolled samples were annealed at 550 °C for 24 h followed by 1 °C min⁻¹ cooling under Ar atmosphere. Small test-pieces with cross-sections of ~ 80 mm² were extracted from the centre of the samples for detailed and representative microstructural investigation.

Microstructural analysis was carried out by using polarized light imaging and electron backscattered diffraction (EBSD). Both techniques require a highly polished but deformation-free surface finish, which was achieved by light grinding, followed by diamond paste and colloidal silica polishing. To improve EBSD efficiency, H₂O₂ was added to the 0.05 μ m colloidal silica suspension and in addition intermediate etching using 5% HF, 35% HNO₃ and 60% H₂O was carried out during the final polishing. EBSD mapping was carried out with a FEI Sirion field emission gun scanning electron microscope (FEG-SEM). The FEG-SEM used is equipped with an HKL EBSD system and the data were analysed using the HKL Channel 5 software. EBSD maps were recorded at an operating voltage of 20 kV with a working distance between 13 and 20 mm. A large step size of 15 μ m was used to scan a large enough area (~ 50 mm²) for macrotexture measurements. In addition, detailed EBSD orientation maps were recorded using a step size of 0.2 μ m.

3. Crystal plasticity finite element modelling

Crystal plasticity finite element modelling (CPFEM) has become a common tool to predict texture evolution [23]

caused by plastic deformation. In this work a CPFEM model originally developed by P. Bate [24], which has been used to successfully predict texture evolution in ferritic steel [25], has been used to predict the texture evolution caused by slip. The model uses a predetermined deformation increment approach, where the increment is applied to the domain boundaries after which overall stress equilibrium is calculated via an iterative process using an elastoviscoplastic mechanical model. Plastic deformation is assumed to occur by slip, which is assumed to be rate sensitive according to:

$$\frac{\dot{\gamma}}{\dot{\gamma}_0} = \left(\frac{\tau}{\tau_0} \right)^m \quad (1)$$

where $\dot{\gamma}$ is the slip rate, τ is the resolved shear stress and τ_0 is the instantaneous slip resistance in any given slip system. The rate sensitivity, m , has a small positive value (typically 0.02) for all slip systems. It was assumed that slip occurred in the $\langle a \rangle$ direction on the basal (3 systems) and prismatic planes (3 systems) and in the $\langle c + a \rangle$ direction on the first-order pyramidal planes (12 systems), i.e. a total of 18 slip systems. Single crystal deformation studies in the temperature interval of 22–840 °C indicate that prismatic slip is easiest at all temperatures, although the relative ease of basal slip increases with increasing temperature [26]. Crystals with suitable orientations started to deform by basal slip at ~ 550 °C [26]. Oliver et al. [27] compared intergranular strain data recorded by an in-situ loading experiment using neutron diffraction with data predicted by elastoplastic self-consistent modelling and found that the inclusion of basal slip is essential to obtain good agreement. Pyramidal $\langle a \rangle$ slip was not accounted for in the present model as the combination of experimental and viscoplastic self-consistent modelling work [28] did not indicate the requirement to include this slip mode to successfully predict deformation behaviour and texture evolution. Following the findings in Ref. [29], $\langle c + a \rangle$ slip was considered in the present model. Note that twinning is not included as a deformation mechanism in the CPFEM model as the aim is to predict texture evolution by slip alone.

The initial single crystal hardening parameters were determined by an iterative fitting of an experimental stress vs. strain curve. The values of elastic compliance used were: $S_{11} = 13.51 \times 10^{-6}$ MPa⁻¹, $S_{12} = 10.65 \times 10^{-6}$ MPa⁻¹, $S_{44} = -3.21 \times 10^{-6}$ MPa⁻¹, $S_{33} = -5.38 \times 10^{-6}$ MPa⁻¹ and $S_{13} = 41.73 \times 10^{-6}$ MPa⁻¹. The initial slip resistance was 112 MPa for prismatic $\langle a \rangle$, 136 MPa for basal $\langle a \rangle$ slip and 760 MPa for pyramidal $\langle c + a \rangle$. The single crystal hardening law parameters were determined by fitting the experimental lattice strain evolution and stress vs. strain curves. A discrete polycrystalline aggregate was modelled as a mesh of 20 node, isoparametric brick elements each with 8 integration points. A representative volume element of $15 \times 15 \times 15$ grains representing the prior rolling (β -quenched) texture of ZIRLO™ was used. To simulate rolling, plane-strain boundary conditions were used. The strain increment size adopted for the simulations was 0.001.

Table 1. Nominal chemical composition of ZIRLO™.

Zr	Nb	Sn	Fe	O
Balance	1.02–1.04 wt.%	0.96–0.98 wt.%	0.094–0.105 wt.%	900–1200 ppm

4. Results

4.1. Microstructural evolution

Rolling at 550 °C to a reduction of 60% and annealing transforms a typical β -quenched microstructure into a bimodal microstructure made up of equiaxed grains. The main features of these microstructures and those at intermediate stages are outlined below.

4.1.1. β -quenched

The β -quench process resulted in a typical Widmanstätten microstructure with prior β grains of 0.5–1 mm in diameter, as shown in Fig. 1a and b. These figures show different α lamellae sizes and the maximum lamellae width observed is $\sim 3.5 \mu\text{m}$. The average diameter of the equivalent area circles which match the areas of the lamellae is $2.1 \mu\text{m}$.

4.1.2. Following 10% reduction by rolling and annealing

Microstructural images of the material after 10% reduction by rolling and annealing are shown in Fig. 1c and d. The images show that some prior β grains are nearly unchanged (Fig. 1c) while others show evidence of lamellae break-up (“a” in Fig. 1c and d), as well as the formation of equiaxed grains (“b” in Fig. 1d). In addition, there are also twin-like features present in the microstructure (“c” in Fig. 1c and d).

4.1.3. Following 20% reduction by rolling and annealing

Fig. 1e and f show the microstructures of the material deformed by 20% rolling reduction and annealed. The micrographs display a mixture of deformed α lamellae in some β grains, whereas others show equiaxed α grains of different sizes. The microstructure is highly heterogeneous with some areas still showing a fully lamellar microstructure and no equiaxed grains.

4.1.4. Following 40 and 60% reduction by rolling and annealing

Following 40% reduction and anneal, the α grain morphology is more homogeneous than after 10% and 20% reduction with no sign of prior β grain boundaries, as can be seen Fig. 1g and h. The lamellae have been replaced by a bimodal population of nearly equiaxed grains. The microstructure is made up of irregular shaped clusters of fine grains (average grain size = $1 \mu\text{m}$) surrounding clusters of larger grains (average grain size = $5.2 \mu\text{m}$). These microstructures are similar to those observed in Zircaloy-4 that had been β quenched and processed (uniaxial compression and tension) in the upper α -phase range (500–750 °C) [10,11]. The large equiaxed grains are smaller after 40% reduction than after 20% reduction. Following 60% reduction and anneal, the microstructure (Fig. 1i and j) is very similar to that after 40%, but the mean grain size is slightly smaller.

4.2. Macrotexture evolution

The crystallographic texture of the materials changes considerably, from a relatively strong β -quenched texture to a relatively weak rolled and recrystallized texture after 60% reduction by rolling.

4.2.1. β -quenched

The α texture of the β -quenched material prior to rolling is shown in Fig. 2a using 0002 and 11 $\bar{2}$ 0 pole figures. The transformation texture is not random; in fact it is rather strong with a maximum pole intensity of 12 times random. Despite that, the Karn’s factors are 0.33 for all three directions, Fx, Fy and Fz. This suggests a $\beta \rightarrow \alpha$ transformation from a strong prior β texture with orthogonal symmetry. The observed texture components correspond to α variants of two major β orientations, in Euler angles: ($\phi 1 = 45^\circ$,

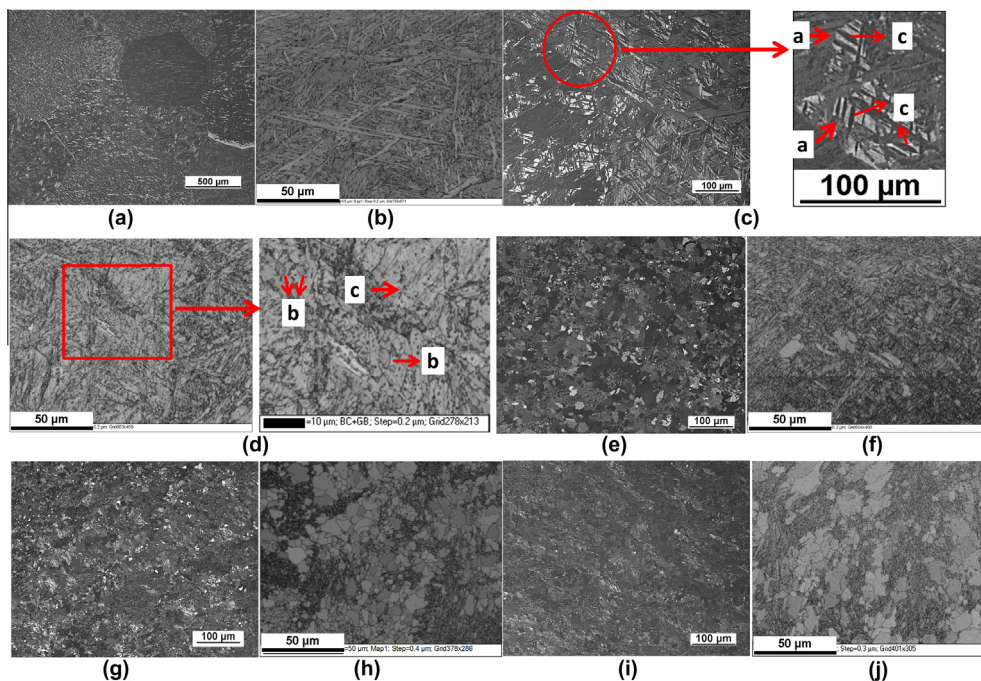


Fig. 1. Microstructure presented by polarized light imaging and EBSD-derived band contrast maps of (a, b) initial β -quenched ZIRLO™, (c, d) after 10% reduction, (e, f) after 20% reduction, (g, h) after 40% reduction and (i, j) after 60% reduction. All rolling trials were carried out at 550 °C and annealed at the same temperature.

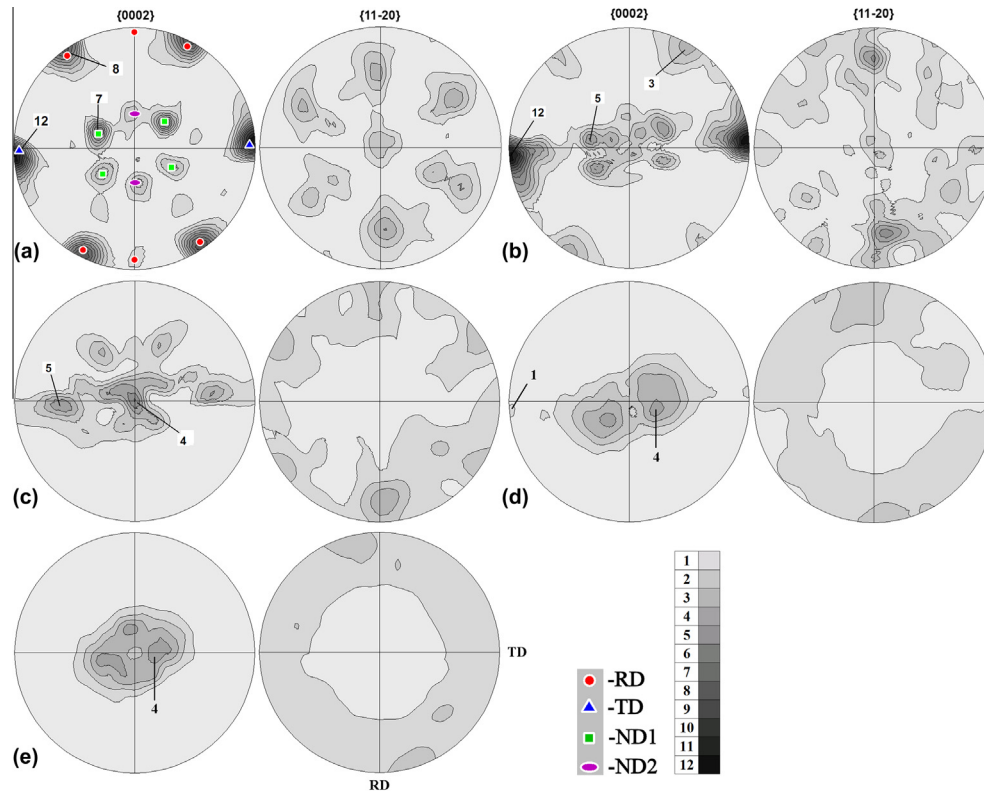


Fig. 2. {0002} and {11 $\bar{2}$ 0} pole figures of (a) β -quenched starting microstructure and after (b) 10%, (c) 20%, (d) 40% and (e) 60% hot-rolling reduction. Note that all rolled material was annealed at 550 °C before texture measurements were carried out.

$\Phi = 0^\circ$, $\varphi_2 = 0^\circ$) and ($\varphi_1 = 90^\circ$, $\Phi = 55^\circ$, $\varphi_2 = 45^\circ$) [30]. The α texture components can be grouped into four main components, depending on the alignment of the 0001 direction: the RD components, the TD components and the ND1 and ND2 components. The RD set is made up of a weak texture component parallel to rolling direction and a stronger component that gives strong pole intensities at $\pm 30^\circ$ from the rolling direction towards the transverse direction. The TD set gives strong ($12 \times$ random) 0002 pole intensities along the TD. The near ND set is made up of the ND1 components, which give pole intensities of $7 \times$ random at $\pm 30^\circ$ from the normal direction towards rolling and transverse directions and weaker ND2 components that give intensity maxima at $\pm 30^\circ$ from the normal direction towards the rolling direction. For clarity, the main components in these texture sets have been indicated on the {0002} pole figure in Fig. 2a and on the orientation distribution function sections shown in Fig. 3a. The Euler angles corresponding to these texture components are given in Table. 2.

It is worthwhile noting that the starting microstructure has several well-defined texture components. This is a significantly different starting point from that of other hot rolling studies (e.g. [31]), which begin with rolled and recrystallized material and the initial texture resembles the final texture, exhibiting two main texture fibres: $\{hkil\}\langle 10-10 \rangle$ and $\{hkil\}\langle 11\bar{2}0 \rangle$.

4.2.2. Following 10% reduction by rolling and annealing

After 10% reduction, the main changes in texture are a weakening of the RD components and no change in the strength of TD components (Fig. 2b). In addition, the ND1 and ND2 texture components become less sharp

and the 0002 pole maxima shift towards the transverse-normal plane and spread towards TD. The changes in the ND1 and ND2 texture components can be best appreciated in the ODF sections (Fig. 3b), which clearly show the generation of new components close to $\varphi = 0^\circ$ and how these are connected to ND1 and ND2. The new texture components appearing close to the ND1 and ND2 components are $\sim 20-40^\circ$ apart from ND1/ND2 ($\varphi_1 = 30$ and 90° sections of Fig. 3b). A weakening of both the ND2 components ($\varphi_1 = 90^\circ$ sections) and the RD components ($\varphi_1 = 60$ and 90° sections) is also evident in Fig. 3b. There is also bridging of nearby texture components close to $\Phi = 0^\circ$ leading to the formation of a fibre texture.

4.2.3. Following 20% reduction by rolling and annealing

Overall, the texture weakens significantly after 20% reduction. The RD texture components fade completely and there is a significant decrease in the TD pole intensities of the {0002} pole figure (Fig. 2c), with the maxima now lying 30° away from TD towards ND. These changes are even clearer in the ODF sections shown in Fig. 3c, which clearly show the weakening of the TD fibre and the movement towards ND. The spreading of ND1 and ND2 orientations around the normal direction observed after 10% reduction continues. In addition, the fibre at $\Phi = 0^\circ$ (Fig. 3c) continues to strengthen, which is accompanied by the development of near ND texture components at ($\varphi_1 = 0^\circ$, $\Phi = 0^\circ$, $\varphi_2 = 0^\circ$) and ($\varphi_1 = 30^\circ$, $\Phi = 0^\circ$, $\varphi_2 = 30^\circ$).

4.2.4. Following 40% reduction by rolling and annealing

Following 40% rolling reduction the texture weakens markedly, with the TD texture component all but disap-

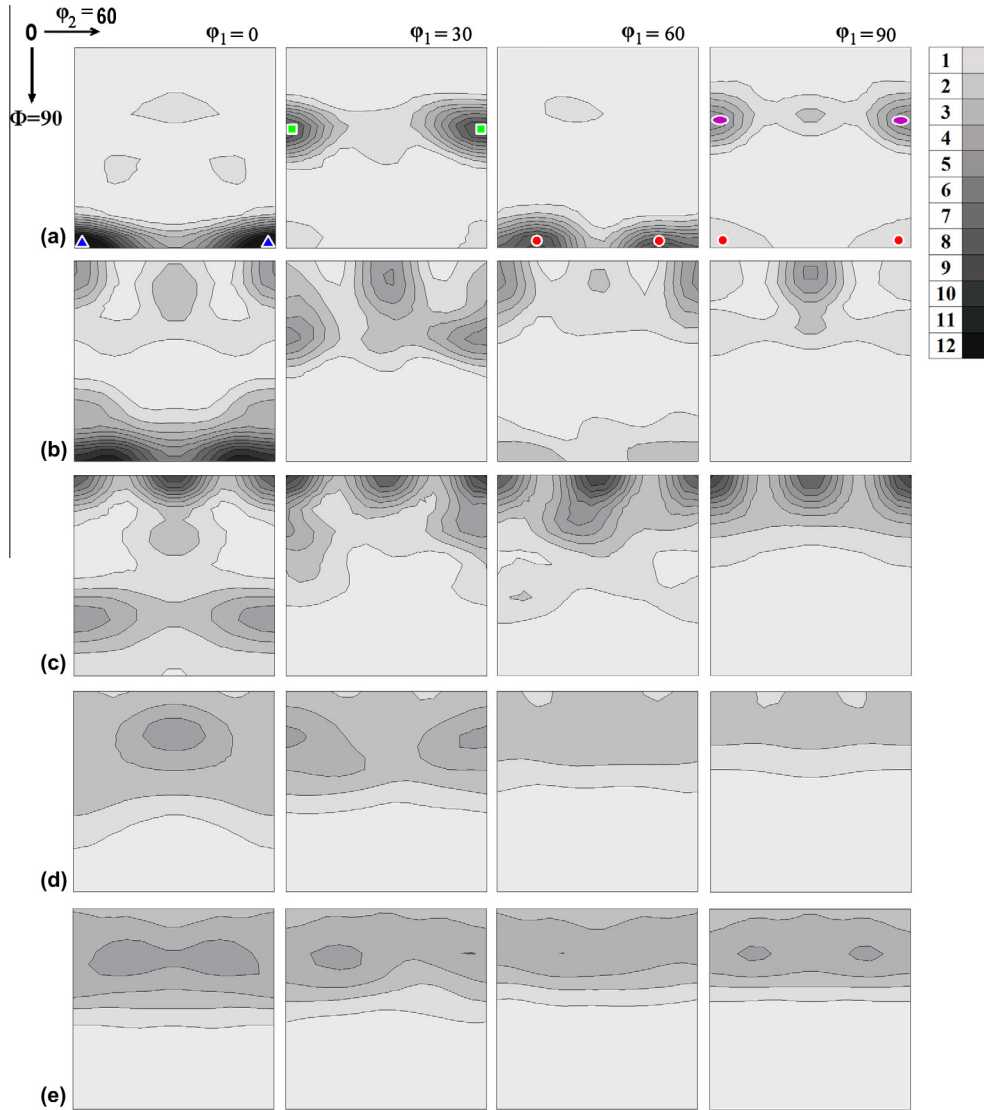


Fig. 3. ODF sections (ϕ_1 constant) of (a) β -quenched starting microstructure and after (b) 10%, (c) 20%, (d) 40% and (e) 60% rolling reduction at 550 °C. Note that all rolled material was annealed at 550 °C before texture measurements were carried out.

Table 2. Representation of texture components by Euler angles.

Texture components	RD			TD	ND1	ND2
	Component 1	Component 2	Component 3			
Euler angles	(90,90,0)	(60,90,45)	(60,90,15)	(0,90,0)	(30,37,0)	(90,33,0)
(ϕ_1, Φ, ϕ_2)	(90,90,60)			(0,90,60)	(30,37,60)	(90,33,60)

pearing (Figs. 2d and 3d) and the 0002 maximum along ND splitting into two significantly weaker maxima at $\pm 15^\circ$ towards TD (Fig. 2d). The ODF sections clearly show that the texture at this stage is weak, and that these two maxima correspond to a weak fibre with a new maximum at $\Phi = 15^\circ$. This fibre is typical of Zr alloys following cold rolling [31], only the texture here is much weaker.

4.2.5. Following 60% reduction by rolling and annealing

Following a 60% reduction, the texture strengthens slightly with a sharpening of the ND fibre in Φ (Figs. 2e and 3e) and a spreading along ϕ_1 . The peak in the $\phi_1 = 0^\circ$ section is replaced by two weaker maxima which

spread along ϕ_1 . This represents a “rotation” about the c-axis, which is often observed following recrystallization [31] of cold rolled Zr alloys. Therefore, despite the very different, non-random starting texture, the texture after 60% reduction of the β -quenched material by rolling and annealing is very similar to that in Ref. [31], where the starting texture was very similar to the final texture.

4.3. Microtexture evolution

In order to understand the mechanisms behind the observed changes in texture and microstructure detailed

EBSD analysis was carried at the different levels of rolling reductions and recrystallization heat treatment.

4.3.1. Misorientation distribution

Before presenting the orientation maps, it is informative to study the evolution of misorientation distribution at the different stages of deformation. The β -quenched microstructure shows, as expected, several characteristic misorientation peaks (Fig. 4), most of which have been reported before for Ti [32] and Zr [33]. These peaks arise naturally from the Burgers orientation relationship between the β and α phases. The common misorientation angles and the corresponding misorientation axes reported in the literature [32,33] are $10^\circ \langle 0001 \rangle$, $60^\circ \langle 11\bar{2}0 \rangle$, $60.8^\circ \langle 1.38 - 1.2.38 0.39 \rangle$, $63.3^\circ \langle 10.5.5.3 \rangle$ and $90^\circ \langle 1 - 2.38 1.38 0 \rangle$ and are highlighted in Fig. 4. In addition, a weak peak corresponding to $20^\circ \langle 0001 \rangle$ can also be seen for the β -quenched microstructure. After 10% reduction, there is a noticeable decrease in the intensity of most peaks and the appearance of new peaks at about 30° and 87° . With increasing deformation there is a noticeable increase in the baseline intensity of the profile, which indicates an increase in the number of random grain boundaries, an increase in the number of low angle grain

boundaries ($<5^\circ$) and strengthening of the 30° misorientation peak. After 60% reduction, nearly all peaks present in the initial β -quenched profile have disappeared, apart from the peak at 30° . This includes the peak at 87° , which corresponds to twin grain boundaries and appears immediately after 10% reduction.

4.3.2. Orientation maps

4.3.2.1. β -quenched. The EBSD map representative of the β -quenched microstructure is displayed in Fig. 5. It shows that the microstructure is composed of interpenetrating α laths with different crystallographic orientations. It is interesting to note that the α laths of different variants contributing to the RD, ND1 and ND2 texture components randomly interpenetrate each other, whereas those contributing to TD texture component seem to lie in clusters of laths with very similar orientations with the common misorientation corresponding to 10° (i.e. $10^\circ \langle 0001 \rangle$). Thus, with the exception of the 10° misorientation peak, all peaks in the misorientation profile shown in Fig. 4 originate exclusively from the variants contributing to the RD, ND1 and ND2 components. The misorientation within each lath is $<2^\circ$.

4.3.2.2. Following 10% reduction by rolling and annealing.

After 10% rolling reduction, although the original structure is still visible, there is clear evidence that the laths are starting to break up, as can be seen in Fig. 6. The random interpenetration arrangement of RD with ND1 and ND2 orientations, evident in the initial microstructure (Fig. 5), has started to change. The α laths are distorted with high levels of stored energy, as can be seen in the inverse pole figure (IPF) map (Fig. 6a).

There appear to be two different types of lath break-up. The first is the occurrence of long, twin-like grains breaking the parent laths. These twins give rise to the 87° peak that appears in the misorientation profile in Fig. 4 and can be indexed as $\langle 11\bar{2}0 \rangle$ twin boundaries. From the EBSD maps (Fig. 6a–c) we observe that this $\langle 11\bar{2}0 \rangle$ twinning leads to three types of grain reorientation (always by 85°): type I = rotation from RD to $\pm 30^\circ$ from normal to transverse direction (NT30 texture component); type II = rotation

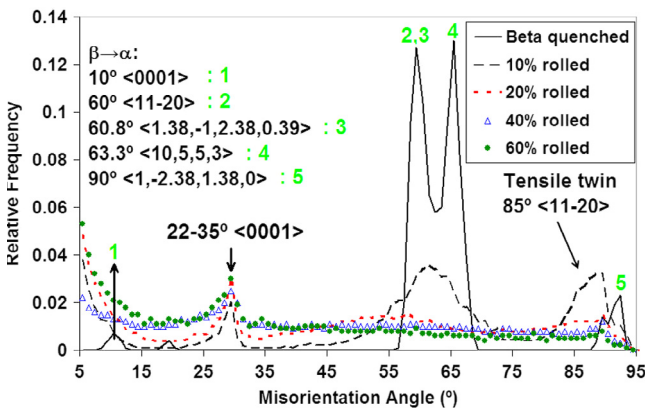


Fig. 4. Relative frequency vs. misorientation angle profile for initial material and after different rolling reductions.

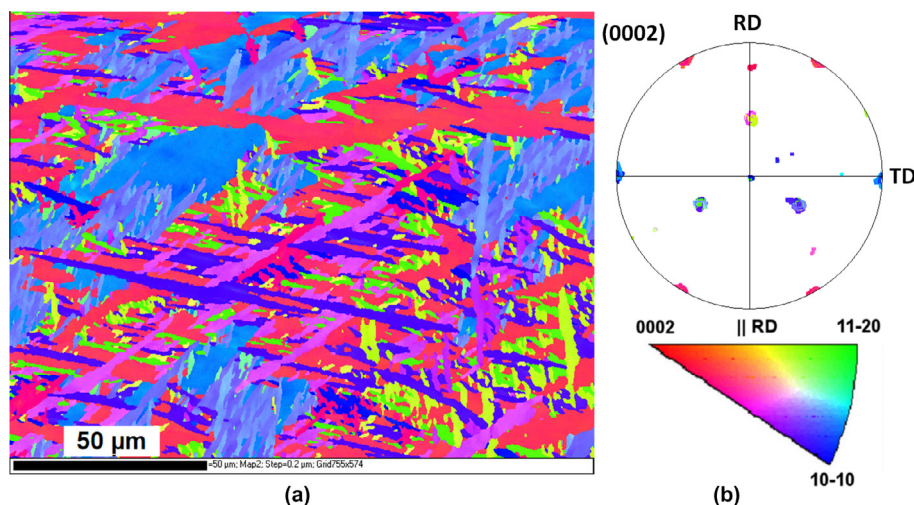


Fig. 5. The β -quenched microstructure: (a) EBSD inverse pole figure map with the corresponding $\{0002\}$ pole figure, and (b) hkl orientation code, corresponding to all the IPF maps presented in this paper.

from TD to ND2; and type III = rotation from TD to RD. Examples of these are shown in the maps in Fig. 6, where the respective twin boundaries are marked as white, red and yellow lines in the IPF/boundary maps. Among the twins from parent TD lamellae, type II twins (Fig. 6e) appear to be wider than type III twins (Fig. 6f). There are examples of interaction between type II and type III twins (Fig. 6f, indicated with an arrow) as well as double twinning (Fig. 6g). Although all three twin types can be identified, the type I twin (white boundary) mode is particularly dominant as can be seen in the micromaps in Fig. 6a and b. This is consistent with the macrotexture data. In fact, the strengthening of the component close to the rolling direction in the pole figure $\{11\bar{2}0\}$ (Fig. 2a) following 10% reduction appears to be a direct result of reorientation by type I twinning. Type I twins make up ~9% of the area of the measured EBSD map after 10% reduction. The small changes in the TD group (Figs. 2a,b and 3a,b), on the other hand, are consistent with the low fraction of other twin modes observed. Apart from the $85^\circ \langle 11\bar{2}0 \rangle$ tensile twin, there is no evidence of other tensile or compressive twins.

The second mechanism responsible for the lamellae break-up is the formation of small, new grains in the deformed parent lamellae. These grains have a well-defined misorientation $\sim 30^\circ$ ($22\text{--}35^\circ$ about $\langle 0001 \rangle$) relative to the parent lamellae, which accounts the $\sim 30^\circ$ peak in the misorientation profile (Fig. 4). This misorientation is commonly observed in α -Zr and its alloys after deformation and recrystallization [21,31]. These grains mostly appear near or at the interface between lamellae. The grain boundaries with a misorientation of $22\text{--}35^\circ$ around $\langle 0001 \rangle$ are labelled in black in Fig. 6a and b, and an example is presented in Fig. 6h. The misorientations of these recrystallized grains with the parent deformed lamellae appear to be defined by rotations about the $\langle c \rangle$ -axis between $\langle 10\bar{1}0 \rangle$ RD and $\langle 11\bar{2}0 \rangle$ RD, depending on the initial lamellae orientation, similar to those observed by Isaenkova et al. [20]. This is similar to the changes in texture observed during static recrystallization of α -Zr following cold rolling [31,34,35], where reorientation from $\langle 10\bar{1}0 \rangle$ RD to $\langle 11\bar{2}0 \rangle$ RD is reported. Other than the recrystallized grains rotated around $\langle 0001 \rangle$, there are also a smaller number of grains tilted from their parent orientations towards the normal direction with and without c -axis rotation.

In summary, the microstructure after 10% reduction contains twins, deformed lamellae and a small fraction of very small, strain-free, recrystallized grains inside and at the boundaries of partially broken-up, deformed parent lamellae. It is also interesting to note that the lamellae contributing to the TD group (blue regions in the map of Fig. 6a) do not show any evidence of recrystallization at this stage.

4.3.2.3. Following 20% reduction by rolling and annealing. The break-up of the parent lamellae continues with 20% reduction. By this stage, nearly all the lamellae have been broken up into smaller grains (Fig. 7), many of which have new orientations. The average grain size remains fairly constant with an average of $1.3 \mu\text{m}$. Twin boundaries are still visible in the large grains contributing to the RD texture components and are identified by a white boundary in the IPF/grain boundary maps in Fig. 7a and b.

These maps also show that the microstructure is now made up of recrystallized fine grains (grains with a black boundary) and larger recovered or recrystallized grains making up a trimodal microstructure. These large grains have mainly ND orientations and appear to be growing at the expense of the deformed neighbouring microstructure. In addition, there is evidence of discontinuous recrystallization in the lamellae contributing to the TD component (Fig. 7b). This suggests that recrystallization in TD oriented grains occurs later than in other initial components. Interestingly, in Fig. 7, there appears to be a strong RD component, which is not observed in the macrotexture. This is just a result of the smaller area sampled and suggests that the microstructure is somewhat heterogeneous.

4.3.2.4. Following 40% and 60% reduction by rolling and annealing. At 40% reduction, a bimodal equiaxed grain structure is well established, as can be seen in Fig. 8a and b. The coarser, recrystallized grains have almost no internal misorientation and contribute mostly, although not solely, to the pole maxima near normal direction. To study this in more detail the grains were divided into fine ($< 2 \mu\text{m}$) and coarse grains ($> 2 \mu\text{m}$). The fine grains contain a greater variety of orientations, as can be seen in Fig. 8 where the orientation spread of the coarse grains and fine grains (Fig. 8c) is shown. Misorientation within the grains is lower at 40% reduction than at 20% and the coarse grains are almost completely strain free whereas the fine grains are not. At 60% reduction, the microstructure is very similar to that following 40%. Both coarse and fine grains have a narrower range of orientations, with most grains contributing to near ND components. Surprisingly, twin boundaries can still be seen, exclusively in the fine grain zone. The average grain size remains unchanged following 40% and 60% reductions.

4.4. CPFEM

CPFEM was used to simulate the contribution of slip to the evolution of texture during rolling. Fig. 9 shows the pole figures predicted for reductions of 10%, 20%, 40% and 60%. As expected, the predicted changes in texture caused by slip are very gradual. After 10% reduction, the pole figures are nearly identical to those in the initial state (Fig. 9b). Following 20% rolling reduction, the positions of the 0002 pole maxima remain unchanged although the pole intensities decrease, indicating randomization of the texture. Interestingly, the intensity drop is larger for the poles aligned with TD than those aligned close to RD. There is also a notable decrease in intensity of the $11\bar{2}0$ poles, with the exception of the maximum along ND, which stays essentially unchanged. With further reductions, it appears that the maxima close to ND move toward RD and that those along TD all but disappear. In summary, the evolution of texture simulated by the CPFE model differs from that observed experimentally in several important ways: it is much more gradual than observed. It underpredicts the intensity of the $\langle 0001 \rangle$ ND components and it predicts the appearance of a $\langle 0001 \rangle$ RD fibre that is not observed. Although it can predict the disappearance of the $\langle 0001 \rangle$ TD component, the decrease in intensity predicted is faster than observed at first and then slower at further reductions, without predicting the move towards ND.

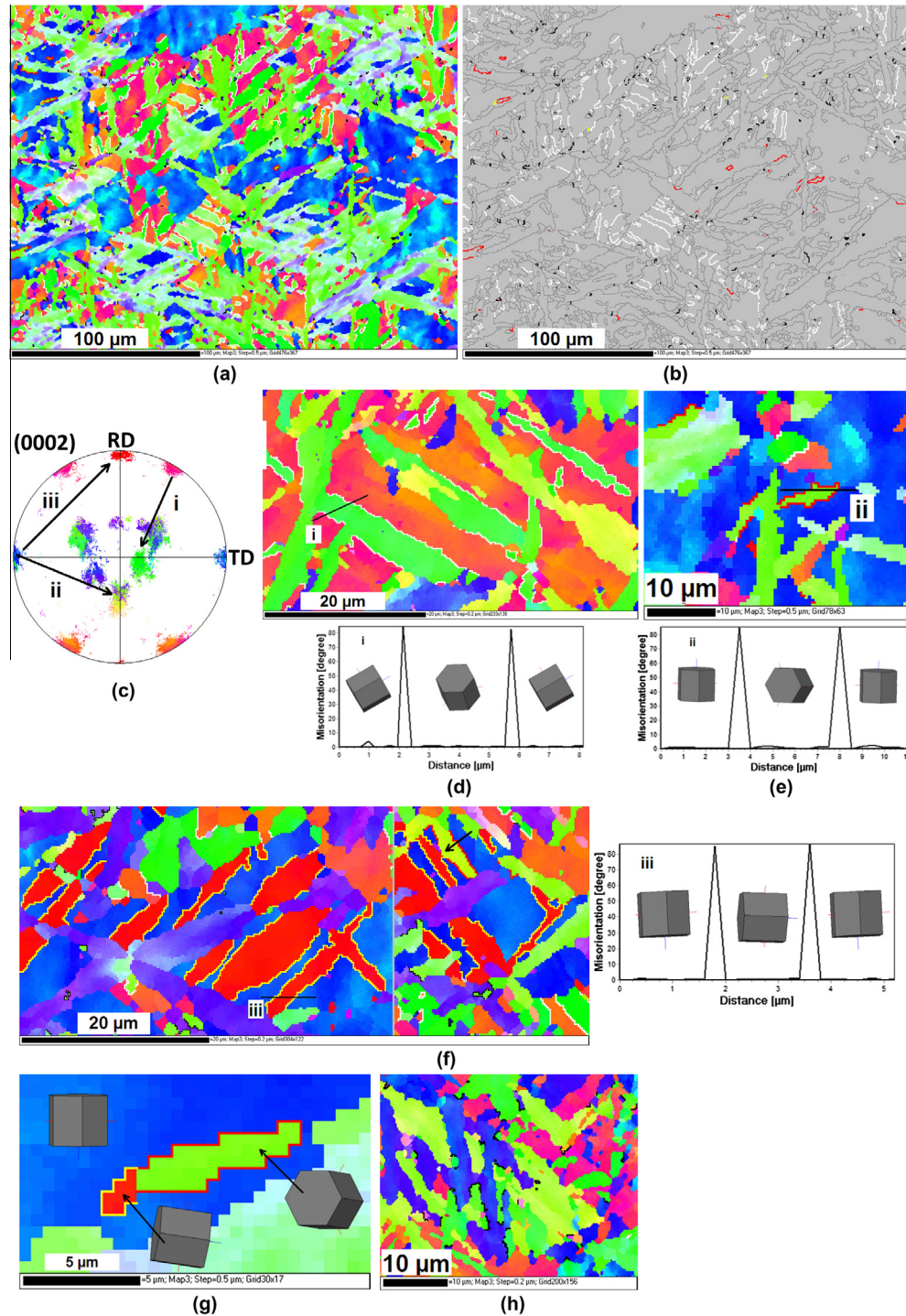


Fig. 6. EBSD maps, {0002} pole figure and animation of crystal orientations after material was deformed by 10% reduction: (a) IPF map highlights 22–35° $\langle 0001 \rangle$ recrystallized grain boundaries (in black) and 85° $\langle 11-20 \rangle$ tensile twin boundaries (white, red and yellow: described below); (b) as (a) but high-angle grain boundary ($>15^\circ$ in dark grey) instead of IPF colouring; (c) the different twin modes of 85° $\langle 11-20 \rangle$ are highlighted in crystal spread and the corresponding examples are given: (d) type I RD \rightarrow ND (white), (e) type II TD \rightarrow ND2 (red) and (f) type III TD \rightarrow RD (yellow). (g) shows the presence of 85° $\langle 11-20 \rangle$ double twinning (type II followed by type III) in the material and (h) shows recrystallized grains outlined by a “special” 30° grain boundary (black), mainly at the interface between lamellae. (For interpretation of the references to colour in this figure legend, the reader is referred to the web version of this article.)

5. Discussion

Our results show that the microstructural evolution during the hot rolling of ZIRLO™ is a result of the complex

interaction between deformation and annealing. There is clear evidence that, even at these elevated temperatures, the deformation in α -Zr alloys takes place by a combination of slip and twinning. We have also found evidence of

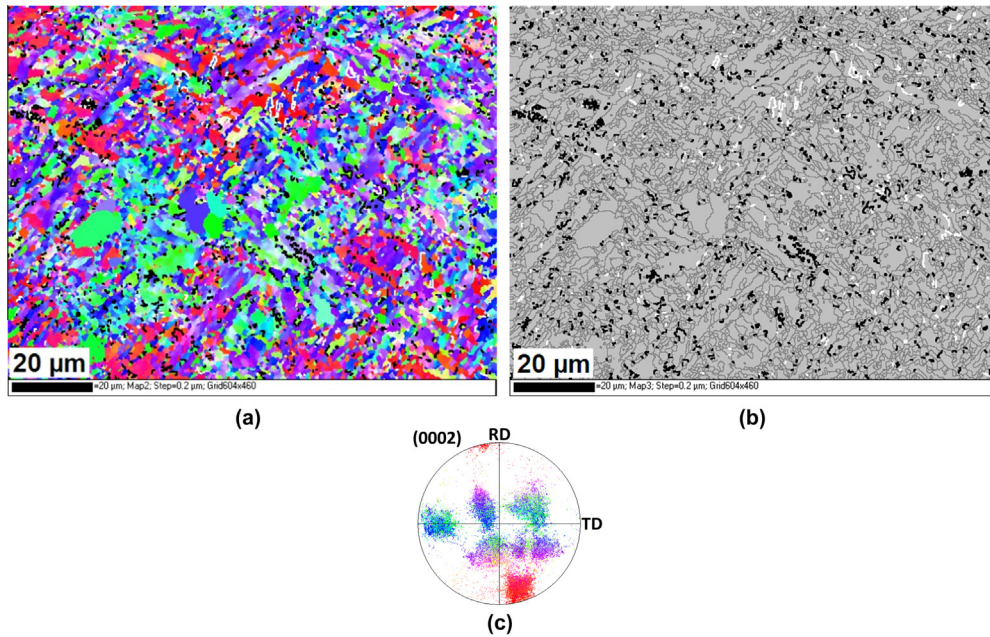


Fig. 7. The highly frequent recrystallized grains $22\text{--}35^\circ$ $\langle 0001 \rangle$ (black boundary) and the 85° $\langle 11\text{--}20 \rangle$ tensile twins (white boundary) are highlighted in (a) the IPF map and (b) the high-angle boundary ($>15^\circ$ in grey) map of material rolled to 20% reduction. In (c) the pole figure is represented using the colour code of the IPF map. (For interpretation of the references to colour in this figure legend, the reader is referred to the web version of this article.)

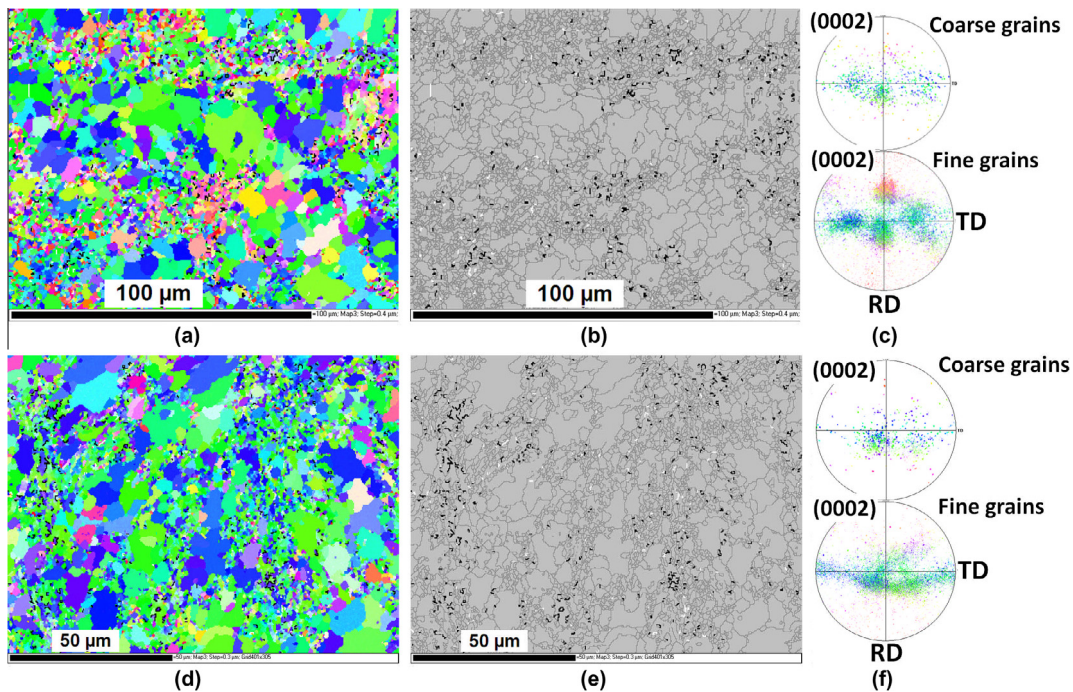


Fig. 8. Recovered large grains and recrystallized fine grains with $22\text{--}35^\circ$ $\langle 0001 \rangle$ recrystallized grain boundaries (black) and twin boundaries (white) highlighted using IPF map (a, d) and high-angle boundary ($>15^\circ$ in grey) map (b, e) for samples after 40% (a–c) and 60% (d–e) reduction. The crystal spread (c, f) corresponding to coarse grains and fine grains are highlighted for 40% and 60% rolled material, where the discrimination between coarse and fine grains is based on the morphological variations noticed in the band contrast maps (Fig. 3b,d).

extensive recovery and recrystallization taking place at 550°C , although it is difficult, from these experiments, to determine how much of this happens dynamically, i.e. during deformation or during the heat treatment after each hot rolling step.

5.1. Deformation by slip

Deformation by slip changes the microstructure in two principal ways: it changes the dislocation density in the material and it changes the texture by grain rotation. These

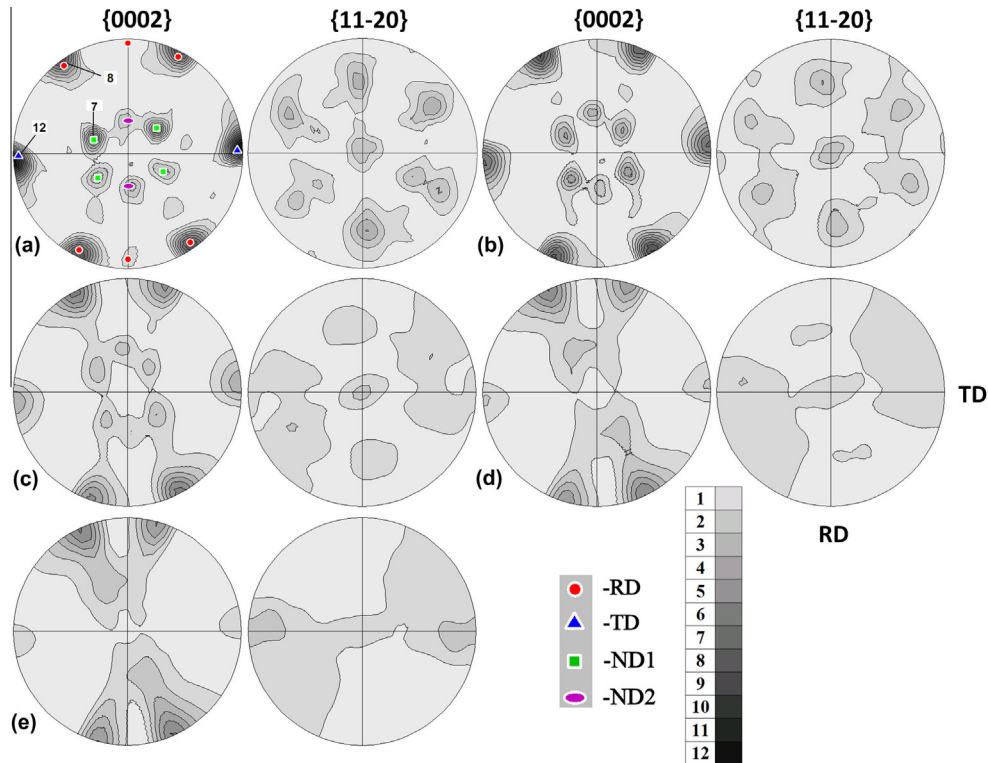


Fig. 9. $\{0002\}$ Pole figures of (a) initial β -quenched condition and CPFEM-predicted pole figures after (b) 10%, (c) 20%, (d) 40% and (e) 60% reduction. Basal $\langle a \rangle$, prismatic $\langle a \rangle$ and pyramidal $\langle c + a \rangle$ slip are the only deformation modes considered in this model.

two effects are not entirely independent, since lattice rotation within grains can give rise to large misorientations and the formation of sub-grains, especially at high temperatures via dynamic recovery. The highly anisotropic nature of slip in zirconium means that grains with different orientations will have very different dislocation activities during deformation [2,36–38]. These differences cause considerable differences in stored energy in different texture components. However, it is difficult to interpret differences in stored energy caused during deformation alone from post-mortem EBSD maps because recovery, which takes place during deformation and the subsequent anneal, is also likely to be orientation dependent.

If grain distortion and the number of low angle boundaries is used as an indicator of stored energy, then it appears that stored energy is higher after the earlier stages of reduction than after larger reductions. This is mostly a consequence of the greater degree of recrystallization that takes place after the larger reductions. At any given reduction, however, the distribution of stored energy is not homogeneous. The EBSD maps appear to show that grains with near ND orientations have lower intergranular misorientation at every stage of deformation. At the later stages, this could be a consequence of recrystallization, but even after just 10% reduction, the lamellae belonging to the ND components show a smaller number of low angle grain boundaries than those contributing to the TD and near RD components (Fig. 10).

In simple terms, the single crystal anisotropy of Zr is characterized by easy slip along $\langle hk10 \rangle$ directions and hard slip along $\langle 0001 \rangle$, because prismatic and basal slip occur more readily than $\langle c + a \rangle$ slip. This makes the grains in the ND components the hardest grains, which should

therefore deform less, consistent with the lower number of low angle grain boundaries. It was also observed that ND grains also show a higher volume fraction of near $\sim 30^\circ$ grain boundaries, which appear during deformation, presumably via dynamic recovery. Although these differences are small because of the small level of applied strain, both the higher misorientation and the lower levels of low angle grain boundaries within the ND component grains would increase grain boundary mobility and hence enhance recrystallization of the ND components with respect to the others.

Deformation by slip will also cause the overall texture to change. In order to discuss the texture evolution caused by slip, it is helpful to recall the comparisons made in Section 4.4 between the textures measured and those predicted by CPFEM. The comparison makes clear that the sudden changes in texture observed after 10% reduction cannot be achieved by slip alone. However, it shows that the disappearance of the $\langle 0001 \rangle$ TD components could be, at least in part, due to slip. It also shows that ND components are relatively stable orientations under rolling. One major disagreement between model and measurement is the prediction of RD components, which clearly do not develop in the experimental data. This, together with the sudden changes in texture measured, are a strong indicators that both twinning and recrystallization play important roles in the texture evolution during hot rolling of Zr.

5.2. Deformation twinning

Our results show, unambiguously, that twinning is an active deformation mechanism during rolling of ZIRLO™

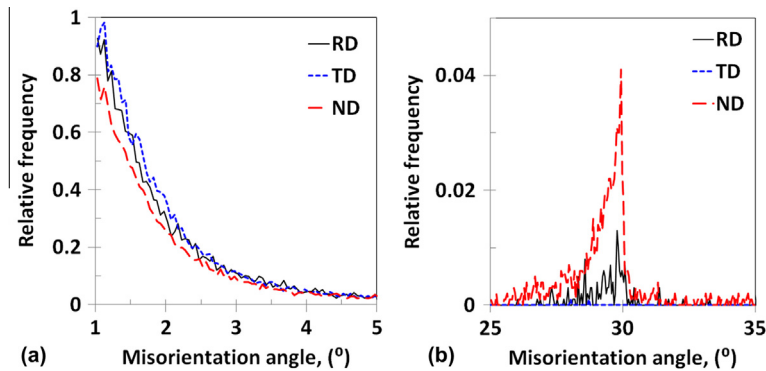


Fig. 10. (a) Relative frequency of low angle grain boundaries after 10% rolling reduction and annealing, consistent with lower strain energy in the lamellae contributing to the ND texture components. (b) Relative frequency of “special” near-30° grain boundaries, showing the opposite trend.

at 550 °C. At the early stages of deformation, it appears to be the mechanism responsible for the disappearance of the $\langle 0001 \rangle$ RD texture components. The most common tensile twinning mode, type I, reorients the grains contributing to the RD components towards ND, as can be seen in Fig. 6c. In addition, twinning appears to be an important mechanism of lamellae break-up. Twinning also generates new (twin) boundaries, which later often act as recrystallization nucleation sites. There is no evidence of twin activity in grains belonging to ND1 and ND2 components, which is consistent with the low Schmidt factor for twinning for these orientations. There is, however, some evidence of twins reorienting grains from TD to ND2 (type II) and TD to RD (type III). In some cases, type III twins effectively reorient grains to near $\langle 0001 \rangle$ ND via type I twins, in a two-step process.

Although the occurrence of twinning is beyond doubt, the relevance of twinning to the development of the final microstructure is harder to ascertain. The relatively high temperature of deformation and the subsequent anneal make it difficult to quantify twinning activity from post-mortem EBSD data. Twin boundaries have high mobility and can therefore disappear during recrystallization. However, if one assumes that the decrease in the $\langle 0001 \rangle$ RD components after 10% is solely due to type I tensile twinning (by far the most common twinning mode and type), this would mean that some 15–20% of the grains are twinned grains. Although this is a significant fraction, the fact that the twinned volumes have near $\langle 0001 \rangle$ ND orientations makes it difficult to determine how important twinning is in determining the final texture. This is because grains with this component seem to grow preferentially during recrystallization, as discussed in the next section.

Nevertheless our results clearly show that twinning does occur during rolling at 550 °C and that it plays an important role in the microstructure evolution of β transformed zirconium, contributing to the break-up of lamellae, recrystallization and accelerating the weakening of the original β -transformed α texture.

5.3. Recrystallization

The last major mechanism of microstructure evolution during rolling at 550 °C is recrystallization. The EBSD maps do not show any large, obviously recrystallized grains after 10% reduction. However, the grain boundary distribution has a peak at ~ 22 – 35° , corresponding to a special high

angle grain boundary that is associated with recrystallized grains following the higher reductions. This is an indication that some recrystallization does occur following 10% reduction and annealing, although the recrystallized grains are very small. It is interesting to note that most of these special grain boundaries, labelled in black in Figs. 6 and 7, are either within or at the border of lamellae with $\langle 0001 \rangle$ ND orientations, which also show lower numbers of low angle grain boundaries. The first clear, non-lamellar, recrystallized grains appear after 20% reduction and annealing. These recrystallized grains clearly nucleate at lamellae boundaries and at twin boundaries, which is consistent with discontinuous recrystallization by strain-induced boundary migration. Some of the recrystallized grains are much larger than average. These larger grains all have $\langle 0001 \rangle$ ND orientations, suggesting that the growth rate during recrystallization, or subsequent grain growth, of these grains is higher than that for other orientations. This is the start of the development of the bimodal microstructure that can be seen following further reduction.

After 40% reduction and annealing, the microstructure is made up almost exclusively of recrystallized grains and the bimodal distribution is well established. The majority of the coarse grains have near $\langle 0001 \rangle$ ND orientations, which again supports the idea that these grains grow preferentially during recrystallization (or subsequent grain growth). Following 60% reduction and annealing, the microstructure consists exclusively of recrystallized grains. The bimodal character of the microstructure prevails, but the microtexture analysis shows that, whereas the coarse grains continue to have mostly $\langle 0001 \rangle$ ND orientations, the finer grains now have the $\langle 0001 \rangle$ direction aligned with the ND–TD trace. This suggests that not only do the $\langle 0001 \rangle$ ND grains grow at the expense of those with other orientations but also implies that the $\langle 0001 \rangle$ ND grains recrystallize to give grains of similar orientation. This recrystallization appears to be a continuous process, akin to recovery, whereby new recrystallized grains form within deformed grains. These new grains are related to the parent deformed grain by a rotation around $\langle 0001 \rangle$ and a slight tilt. It is as if the dislocations generated during deformation rearrange to form subgrains and, eventually, new grains which can then grow. Although this mechanism seems to be operative for all orientations, there seems to be a growth advantage for grains with $\langle 0001 \rangle$ ND, which could be due to the higher number of 22–35° grain boundaries that appear to be formed during deformation, presumably via

dynamic recovery. Mironov et al. witnessed similar behaviour in commercially pure Ti [39]. They suggested a mechanism whereby sub-grain boundaries can evolve into these special high angle grain boundaries through the action of prismatic slip giving continuous recrystallization. Since grain boundary mobility increases with misorientation, this would give the ND component grains an advantage during early recrystallization, leading to preferential growth over other components.

5.4. Morphological changes

The mechanisms responsible for lamellae break-up appear to be twinning and both continuous and discontinuous recrystallization. Twinning generates nuclei for new grains with very different orientations and acts mainly in the $\langle 0001 \rangle$ RD lamellae, whereas continuous recrystallization generates new equiaxed grains but with similar orientations and occurs throughout. Since twinning and recrystallization happen to different extents in lamellae with different orientations, these morphological changes are not homogeneous. Twinning occurs most readily in the lamellae contributing to the $\langle 0001 \rangle$ RD components, whereas the lamellae from the $\langle 0001 \rangle$ TD components are the last to break up. It is this heterogeneity that leads to the formation of the bimodal grain size distribution following 40% and 60% reductions. Recrystallization is dominated by the preferential growth of grains with $\langle 0001 \rangle$ ND orientations. Following 40% reduction, the smaller grains have almost a random texture, but after 60% reduction these smaller grains have near $\langle 0001 \rangle$ ND orientations, suggesting that the larger grains present at 40% break-up with further deformation.

It is also interesting to note that the average grain size does not increase significantly throughout the rolling. In fact, there seems to be a slight decrease in average grain size from 40% to 60% reduction. This further supports the idea that although the $\langle 0001 \rangle$ ND fibre is stable, grains with this orientation continue to break up during deformation. Our experiments suggest this break-up occurs by continuous recrystallization within the grains, with new grains being rotated from each other around $\langle 0001 \rangle$, with a slight tilt of the $\langle 0001 \rangle$ direction away from ND. Further work is underway to determine the mechanism of grain break-up and how it arises from the prismatic slip that dominates deformation at this stage. This mechanism is also likely to a contributing factor to the development of the $\langle 0001 \rangle$ ND fibre earlier on.

6. Conclusions

The aim of this detailed study on the microstructure evolution of ZIRLO™ during hot rolling was to develop an understanding of the physical processes responsible for transforming a β -quenched lamellar microstructure with its characteristic texture into the typical hot rolled microstructure, made up of equiaxed grains and with a basal-normal texture. Our work showed that slip, twinning and recrystallization are all instrumental in the changes of both grain morphology and texture.

At 550 °C, the deformation in ZIRLO™ takes place by a combination of slip and twinning. Slip is responsible for most of the deformation; however, for much of the material, the effects of slip on texture and microstructural changes

are in great part indirect, via recrystallization. The most important aspect of slip seems to be its anisotropy and the effect this has on the homogeneity of deformation and on the distribution of low angle grain boundaries and special 22–30° grain boundaries. This is particularly evident in the β -quenched material we studied, the texture of which was made up of distinct texture components, each with different slip activities.

Twinning is not only an active deformation mechanism during rolling at 550 °C but is also an important mechanism of microstructure evolution. It is almost solely responsible for the fast changes in texture observed within 20% reduction. It is the mechanism responsible for the disappearance of the $\langle 0001 \rangle$ RD texture components and the weakening of the texture observed at the early stages. Twinning is also an important mechanism of lamellae break-up, both during deformation and later during recrystallization, when twins act as nucleation sites.

Recrystallization is important for both lamellae break-up and texture evolution. There is evidence of both continuous and discontinuous recrystallization. During recrystallization, grains with $\langle 0001 \rangle$ ND grow preferentially, acting to strengthen the $\langle 0001 \rangle$ ND fibre, which dominates the final texture.

A successful model for hot thermomechanical processing of β -quenched Zr should include slip, twinning and recrystallization. These mechanisms all combine to give the texture typically found after hot rolling. Although the processing steps used here gave rise to a duplex grain size, this work suggests that the further rolling, with a number of intermediate rolling steps, could give rise to an equiaxed microstructure with a relatively weak texture.

Acknowledgements

We would like to thank Westinghouse for supplying the material and the EPSRC for funding this research. J.Q.d.F. would also like to thank Pete Bate for his guidance, support and inspiration and for writing the programs without which we would have not been able to do this work.

References

- [1] J.R. Davis, Zirconium and hafnium, in: J.R. Davis (Ed.), *Metals Handbook*, ASM International, Materials Park, OH, 1998, pp. 621–623.
- [2] E. Tenckhoff, *Deformation Mechanisms, Texture and Anisotropy in Zirconium and Zircaloy*, ASTM 966, Philadelphia, 1988.
- [3] I. Charit, K.L. Murty, *Mater. Sci. Forum* 539–543 (2007) 3377.
- [4] R.G. Ballinger, G.E. Lucas, R.M. Pelloux, *J. Nucl. Mater.* 126 (1984) 53.
- [5] W. Li, R.A. Holt, *Mater. Sci. Forum* 539–543 (2007) 3353.
- [6] E. Girard, R. Guillen, P. Weisbecker, M. Francois, *J. Nucl. Mater.* 294 (2001) 330.
- [7] B.L. Shen, M. Liu, C. Li, S.Y. Qiu, S.H. Ying, M. Zeng, *Rare Met. Mater. Eng.* 36 (2007) 803.
- [8] S.S. Kim, S.C. Kwon, Y. Suk Kim, *J. Nucl. Mater.* 273 (1999) 52.
- [9] J.K. Chakravarty, G.K. Dey, S. Banerjee, Y. Prasad, *Mater. Sci. Tech.* 12 (1996) 705.
- [10] C. Chauvy, P. Barberis, F. Montheillet, *Mater. Sci. Forum* 467–470 (2004) 1151.
- [11] C. Chauvy, P. Barberis, F. Montheillet, *Mater. Sci. Eng., A* 431 (2006) 59.

- [12] I. Weiss, F. Froes, D. Eylon, G. Welsch, *Metall. Mater. Trans. A* 17 (1986) 1935.
- [13] J.H. Chung, *Scripta Mater.* 61 (2009) 161.
- [14] J. Bingert, T. Mason, G. Kaschner, G. Gray, P. Maudlin, *Metall. Mater. Trans. A* 33 (2002) 955.
- [15] H. Francillette, B. Bacroix, M. Gaspérini, J.L. Béchade, *Mater. Sci. Eng., A* 234–236 (1997) 974.
- [16] S. Kim, *Metall. Mater. Trans. A* 37 (2006) 59.
- [17] W.S. Choi, H.S. Ryoo, S.K. Hwang, M.H. Kim, S.I. Kwun, S.W. Chae, *Metall. Mater. Trans. A* 33 (2002) 973.
- [18] Z. Trojanová, P. Lukác, F. Král, R. Král, F.F. Lavrentev, V.N. Nikiforenko, *Mater. Sci. Eng., A* 137 (1991) 151.
- [19] M.G. Isaenkova, V.P. Pavelko, Y.A. Perlovich, *At. Energ.* 62 (1987) 204.
- [20] M.G. Isaenkova, S.N. Kaplii, Y.A. Perlovich, T.K. Shmeleva, *At. Energ.* 65 (1988) 582.
- [21] F. Gerspach, N. Bozzolo, F. Wagner, *Scripta Mater.* 60 (2009) 203.
- [22] A.V. Nikulina, V.A. Markelov, M.M. Peregud, V.N. Voevodin, V.L. Panchenko, G.P. Kobylansky, *J. Nucl. Mater.* 238 (1996) 205.
- [23] R.J. Asaro, A. Needleman, *Acta Metall.* 33 (1985) 923.
- [24] P. Bate, *Philos. Trans. R. Soc. Lond.* 357 (1999) 1589.
- [25] P.S. Bate, J. Quinta da Fonseca, *Mater. Sci. Eng., A* 380 (2004) 365.
- [26] A. Akhtar, *Acta Metall.* 21 (1973) 1.
- [27] E.C. Oliver, M.R. Daymond, P.J. Withers, *Mater. Sci. Forum* 495–497 (2005) 1553.
- [28] F. Xu, R.A. Holt, M.R. Daymond, *J. Nucl. Mater.* 394 (2009) 9.
- [29] R.J. McCabe, E.K. Cerreta, A. Misra, G.C. Kaschner, C.N. Tome, *Philos. Mag.* 86 (2006) 3595.
- [30] N. Gey, M. Humbert, M.J. Philippe, Y. Combres, *Mater. Sci. Eng., A* 230 (1997) 68.
- [31] K.Y. Zhu, B. Bacroix, T. Chauveau, D. Chaubet, O. Castelnau, *Metall. Mater. Trans. A* 40A (2009) 2423.
- [32] S.C. Wang, M. Aindow, M.J. Starink, *Acta Mater.* 51 (2003) 2485.
- [33] N. Gey, M. Humbert, E. Gautier, J.L. Béchade, *J. Nucl. Mater.* 328 (2004) 137.
- [34] K.Y. Zhu, D. Chaubet, B. Bacroix, F. Brisset, *Acta Mater.* 53 (2005) 5131.
- [35] K.Y. Zhu, B. Bacroix, T. Chauveau, D. Chaubet, O. Castelnau, *Mater. Sci. Forum* 550 (2007) 545.
- [36] E. Tenckhoff, *Z. Metallk.* 63 (1972) 192.
- [37] A. Akhtar, *Metall. Trans. A* 6 (1975) 1217.
- [38] F. Xu, R.A. Holt, M.R. Daymond, *Acta Mater.* 56 (2008) 3672.
- [39] S.Y. Mironov, G.A. Salishchev, M.M. Myshlyaev, R. Pippan, *Mater. Sci. Eng., A* 418 (2006) 257.